32nd Symposium on Naval Hydrodynamics
Hamburg, Germany 5-10 August 2018

A Material and Fluid Scaling Approach to Validate FSI Simulations of Cavitation Interaction with Polymeric Coatings

G. L. Chahine, A. Gnanaskandan, A. Mansouri, C.-T. Hsiao, and R. Content

(DYNAFLOW, INC., USA)

ABSTRACT

Spark-generated bubble and fluid-structure interaction (FSI) simulations are used as experimental and numerical tools to study cavitation effects on polymeric coatings. They are also used to demonstrate that proper bubble dynamics and coating material interaction scaling can be achieved by properly selected geometric, fluid dynamics, and material properties. Here, cavitation bubble dynamics in a high pressure cavitating jet eroding a Polyurea layer is simulated using spark-generated bubbles operating at reduced pressures near an Agar layer of a properly selected concentration. Geometric scaling is based on the ratio of bubble maximum radii in the two configurations. Fluid dynamics scaling follows the Rayleigh scaling, i.e. lengths are normalized by the bubble maximum radius and times by the Rayleigh time. Scaling of the materials properties is achieved by equating the ratios of the materials properties (Young's and shear moduli) with the ratio of the peak pressures generated at bubble collapse. The full FSI numerical simulations show validity of the scaling.

INTRODUCTION

Compliant materials are increasingly used as coatings in naval applications and their resistance to cavitation is an important issue. Cavitation erosion results from the collapse of microbubbles forming shock waves and fast reentrant jets impacting on the material (Hammitt 1980, Brennen 1995, Kim *et al.* 2014). The response of the coatings involves large local accelerations of the material surface and strong feedback and modification of the bubble dynamics itself. However, the small spatial and fast temporal scales prevent adequate experimental measurements of these physical processes. Numerical simulations have investigated the dynamics of bubbles and materials but still require experimental validation (Kim *et al.* 2014, Chahine & Hsiao 2015, Choi & Chahine 2017). In this study, we introduce a scaling approach that makes observation and measurement of the bubble dynamics and the material structural dynamics possible. In lab-scale visualizations, the bubble dynamics is slowed down and the length scales are increased using classical spark-generated bubbles in a vacuum tank (Kling & Hammitt 1972, Chahine *et al.* 1995, Jayaprakash *et al.* 2012). This, however, is not sufficient to properly observe the FSI, and the material of the coating exposed to the full-scale cavitation (e.g. Polyurea in this study) also has to be replaced by a material with mechanical properties scaled down from those of Polyurea to match the level of pressure loadings from the spark-generated bubbles. Thus, in the scaling method presented in this paper, fast collapsing microscopic cavitation bubbles on Polyurea are replaced with centimeter sized slower spark-generated bubbles interacting with Agar at various concentrations. This enables one to validate the numerical FSI simulation procedure, to visualize bubble and material behavior, and to predict the behavior of microscopic bubbles on Polyurea.

In this paper, we describe the various steps of the scaling process. We first discuss the bases of the approach and the experimental and numerical methods used. We then show that the numerical simulations recover the experimental spark-generated bubble results. With this established, we show numerically using normalized plots that the results of the microscopic high-pressure cavitation bubbles collapsing on Polyurea are the same as those obtained in the spark conditions on an Agar layer selected to have the proper material properties. We then discuss the physical parameters, which are not conserved between the scales and which interfere with having a perfect correspondence between scaled conditions.

APPROACH

To scale properly the bubble dynamics, the following scaling has been classically used. The bubble radius - or any selected length on the bubble shape - is

normalized with the bubble maximum radius R_{max}, and time is normalized with the Rayleigh time,

$$T_{Rayleigh} = R_{\max}\sqrt{\rho / P_{amb}}\,, \qquad (1)$$

where ρ is the liquid density and P_{amb} is the local liquid ambient pressure in the vicinity of the bubble. With this normalization, non-dimensional bubble size versus non-dimensional time curves fall on top of each other for all conditions (except for large variations in the internal gas pressures, viscosity or surface tension of the bubbles). This means that one can deduce the dynamics for any condition once only one reference condition is known. A spark-generated test will then provide scaled results for microscopic as well as for meter-sized bubbles (ignoring terms that have been shown to have, in general, secondary effects such as viscosity, gas pressure, and surface tension). Near a rigid boundary, at a distance X from the bubble center, the same scaling applies, provided that the normalized distance, $\bar{X} = X / R_{\max}$, is conserved.

Near a deformable coating layer, this scaling is still valid, provided however, that the thickness of the coating is also scaled with R_{max} and that the ratio between the characteristic impulsive pressure generated by the bubble collapse at the boundary and the ratios of the parameters characterizing the material resistance to the load are the same. The relevant parameters here are the material Young modulus, E, the shear modulus, G, and the bulk modulus, K.

Expressed differently (but in an equivalent fashion), with ρ_m being the material density, the ratios of the following material characteristic times

$$\tau_E = R_{\max}\sqrt{\rho_m / E}\,,$$
$$\tau_K = R_{\max}\sqrt{\rho_m / K}\,, \qquad (2)$$
$$\tau_G = R_{\max}\sqrt{\rho_m / G}\,,$$

and the Rayleigh time, Eqn. (1), should be conserved. This reduces to conserving the ratios:

$$\frac{\rho_m}{\rho}\frac{P_{amb}}{E}, \quad \frac{\rho_m}{\rho}\frac{P_{amb}}{K}, \quad \frac{\rho_m}{\rho}\frac{P_{amb}}{G}. \qquad (3)$$

In this study, we examined Polyurea, which is of interest because of its good performance against shock from explosions. Its resistance to cavitation erosion has been investigated in (Choi & Chahine, 2017) and its relevant material properties are listed in Table 1 (Amirkhizi *et al.* 2006).

For material scaling purposes, we performed large-scale spark tests in the laboratory using various concentrations of Agar, which has been used in studies of biological effects of cavitation (Movahed *et al.* 2016). Agar is a viscoelastic material like Polyurea, and has shear and Young's moduli, which are much smaller than those of Polyurea (Nayar *et al.* 2012). As shown in Table 1, with 5% Agar powder mixed with water, the Young and shear moduli (which are related through the Poisson ratio, $E = 2G(1+\nu)$; $\nu \simeq 0.5$) are about 30 times smaller than the Polyurea values, while the bulk moduli are about the same. However, the numerical simulations presented below confirm that K is less relevant for the present problem, as it relates to time scales much smaller than those involved during the dynamics of the bubble of interest here.

Table 1: Properties of materials.

MATERIAL	PU	Agar 5%	Agar 0.5%	Ratio PU/Ag5%	Ratio PU/Ag0.5%
Young Modulus, E (MPa)	67	2.2	0.134	30	500
Shear Modulus, G (MPa)	22.2	0.73	0.045	30	493
Bulk Modulus, K (MPa)	3000	2370	2370	1.3	1.3
Density (Kg/m^3)	1100	999	992	1.10	1.11

Table 2: Liquid and bubble conditions.

FLUID CONDITIONS	PU	Agar 5%	Ratio PU/Ag 5%	PU	Agar 0.5%	Ratio PU/Ag 0.5%
Pamb (MPa)	3	0.10	30	7	0.014	500
Rmax (mm)	0.1	10	0.01	0.1	20	0.005

Table 1 also shows the properties of a 0.5% Agar mixture. The Young's and shear moduli are in the same range, i.e. ~500 times less than for Polyurea, while the ratio of the bulk moduli is about 1. Changing the concentration of Agar changes the ratios discussed above and thus results in simulating smaller or larger impact loading ranges.

Table 2 compares the local ambient pressures, P_{amb}, between spark-generated bubble test conditions for Agar and a typical pressure in the stagnation region of a cavitating jet impacting on a Polyurea coated plate since cavitating jets are commonly used to test materials for their resistance to cavitation erosion (Chahine *et al.* 2014). Note that the impulsive pressures from cavitation bubble collapse are proportional to the local ambient pressure driving the bubble collapse, P_{amb}. Since the ratio of the erosion resistance characteristics (E, G) of the two materials (Polyurea, Agar) is about 30, for 5% Agar a spark test conducted at a tank pressure of ~0.1 MPa, should scale properly cavitating jet bubble behavior on Polyurea in a ~3 MPa (~450 psi) jet, which is below the threshold for significant damage. However, if 0.5% Agar (where the material resistance ratio increases to ~500) is used at a spark test tank ambient pressure of 0.014 MPa (2 psi), a ~7 MPa (~1000 psi) cavitating jet interaction with Polyurea can be simulated. A whole range of selections is possible to simulate various levels of cavitation erosion on Polyurea by selecting the ambient pressure in the spark tank and the percentage of Agar in the mixture.

EXPERIMENTAL SETUP

Spark bubbles have been used for many decades since the early work of Ellis (1965) to simulate cavitation and underwater explosion bubbles. In the present study, the bubbles are generated by very fast underwater discharge of a high-voltage charge stored in capacitors between two coaxial electrodes. The electrical energy is converted into small volume plasma which has temperatures as high as 20,000°K, and pressures as high as 10^9 Pascals (Kling, 1970). Because of the high pressure, the liquid near the plasma interface is initially compressed. The pressure in the gas sphere then quickly falls but is well above that of the surrounding liquid. From this point on, incompressible hydrodynamic effects dominate. The pressurized gas expands into a relatively large bubble, which subsequently collapses and re-expands. The phenomena preceding the incompressible hydrodynamic phase occur quickly and are accompanied by light generation that prevents accurate determination of the initial bubble radius using conventional high-speed photography. The dynamics of the spark-generated bubbles away from boundaries have been shown to follow the Rayleigh-Plesset equation.

The energy supplied to the spark is controlled by the voltage applied to the capacitor of the spark generator and by the size of the capacitor. In cases where the bubble is significantly far from boundaries, it retains a spherical shape up to the time of maximum volume and a sphere's radius could be easily measured. In cases where the bubble is distorted by the presence of boundaries, an equivalent radius can be derived. Here, it is obtained by assuming the bubble to be axisymmetric and calculating the volume as that of a solid of revolution of the observed outline around an axis of symmetry.

The experimental setup used in this study is illustrated in Figure 1. It consisted of a) a 60 cm × 60 cm × 60 cm Plexiglas tank with thick walls needed to enable one to reduce the ambient pressure well below the atmospheric pressure, b) a spark generator system, which discharges the energy stored in the capacitor across the gap between coaxial electrodes, c) a vacuum pump, d) a high-speed camera and two LED lights, e) a Plexiglas structure inside the tank where the Agar plate and electrode are mounted, and f) a computer system to control the spark energy and synchronize with the high-speed imaging.

To generate larger bubbles and enhance the observation of the bubble-Agar interaction, the tests were performed under low ambient pressure using the vacuum pump. For post-test analysis, the ambient pressure was calculated based on the measured pressure above the free surface in the tank plus the hydrostatic head at the location of the electrodes. The vapor pressure was deduced from the ambient water temperature. An IDT Y-series model high-speed camera was used to record the bubble evolution at framing rates between 3,000 and 10,000 frames per second. A small exposure time of each frame, 90 µs was used to capture the bubble shape and formation of reentrant jet sharply. Two LED lights illuminated the front side of the test tank.

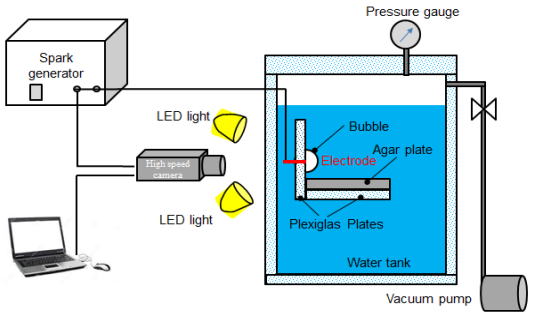

Figure 1: Experimental setup to produce and visualize spark-generated bubbles and their interaction with nearby boundary such as an Agar layer. In this setup, using the principle of images, only half of a bubble is generated to improve visualization. A full bubble over the middle of the plate would produce the same results.

As illustrated in Figure 1, in order to improve the visualization and obtain larger bubbles, the electrodes were located flush with the visualization plexiglass wall, i.e. the wall through which the high-speed movies were recorded. A half-sphere bubble was therefore generated, and because of the principle of images in potential flow, reproduces the behavior of a full bubble after including the image. The effects of the presence of the plane of symmetry wall (surface tension and viscosity) are minimal and have negligible effects on the bubble dynamics and on the visualization. The transparent plane of symmetry wall allows very good recording of the bubble deformation, including good visualization of the reentrant jet (see for example Figure 2 for a bubble in the gravity field).

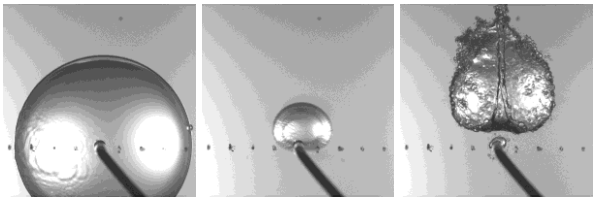

Figure 2. Spark-generated bubble collapse in gravity showing clearly an upward moving reentrant jet.

In addition to visualizing clearly the inside of the bubble, the transparent plane of symmetry allows one to visualize a cut through the Agar coating layer

in the plane of symmetry. We took advantage of this view to evaluate the deformations and strains inside the Agar coating. In order to do so, dark dot particles were inserted as markers and were distributed regularly in the coating thickness and along the axisymmetric bubble/coating configuration radial direction from the axis of symmetry. This can be seen in the movie images shown in Figure 7 (later in the paper) and enabled us to follow the particle motion in time using the high-speed photography and then to deduce deformations, strains, and strain rates.

Spark Generated Bubbles Characterization

The spark generator system used in this work has been extensively used to simulate bubble dynamics and underwater explosion bubbles. The size and period of a generated bubble are directly controlled by the voltage, *V*, used to charge the capacitor, *C*, and by the selected pressure inside the spark tank, P_{amb}. The electric energy delivered is $E_e=0.5CV^2$. However, most of this energy is lost in the sparking and shock wave formation and only about 5% of, $E \simeq 0.05\, E_e$, is actually transferred into the bubble.

Figure 3 illustrates calibration curves for a bubble generated away from boundaries. It shows the maximum bubble radius achieved versus the electric voltage, *V*, for a set of values of the ambient pressure, all with a capacitor of 1μF. For a given voltage, the bubble size increases when the ambient pressure is reduced. Similarly, at a given ambient pressure, the bubble size increase with the voltage.

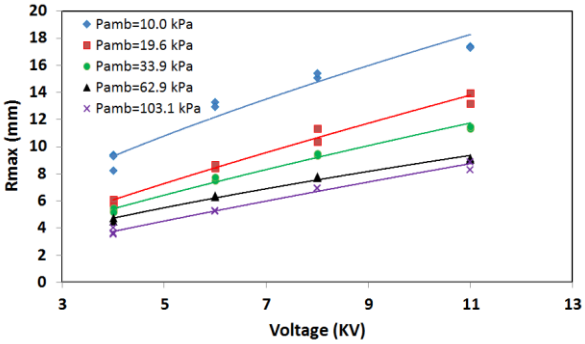

Figure 3: Bubble maximum radius, R_{max}, versus voltage in the spark generating system for different ambient pressure in the test tank.

It is well known for underwater explosion that the maximum bubble radius generated at a given depth, or P_{amb}, is directly proportional to one third power of the ratio of the explosion energy and the depth (Cole, 1965 ; Snay & Christian, 1952),

$$R_{\max} = J_1 \left(\frac{E}{P_{amb}} \right)^{1/3}, \qquad (4)$$

where J_1 is an explosive type dependent constant. This relationship applies also for the spark bubbles, as shown in Figure 4. If we plot R_{max} as a function of the energy in the spark bubble divided by the ambient pressure, E/P_{amb}, all data points from Figure 3 collapse on a single curve, which has a 1/3 power. Note that the R_{max} of the half bubble on the wall is $2^{1/3}$ larger because the energy is deposited to a half sphere. In the figure the corresponding radii were divided by $2^{1/3}$ to correct.

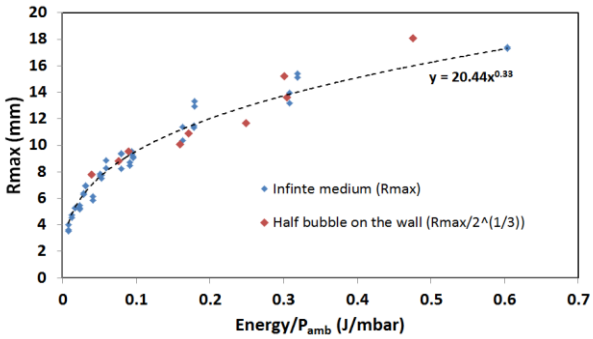

Figure 4: Maximum bubble radius versus the energy, E_e, in the spark divided by the ambient pressure.

FSI NUMERICAL SIMULATIONS MODEL

In parallel to the experimental work, the interaction of a growing and collapsing bubble with a nearby layer of a viscoelastic material was modeled using coupled fluid and structure codes. The fluid was modeled using a multi-component fully compressible flow solver, which is able to capture shock waves and handle liquid gas interfaces. This was coupled with a finite element method structural code. The numerical modeling includes description of the bubble dynamics near the deformable coating and fluid-structure interaction (Chahine, 2014; Chahine & Hsiao, 2015; Choi & Chahine, 2017). Resulting deformations, strains, and stresses in the material were computed and the predictions were compared with the spark-generated bubbles. Additional computations were conducted to demonstrate the validity of the scaling approach described above.

Compressible flow solver

The multi-material compressible Euler equation method used in this study can capture nonlinear acoustic and shock wave propagation in multi-material media by solving the following continuity, momentum, and energy equations in a fixed Cartesian grid (Wardlaw & Luton 2003, Kapahi *et al.* 2015):

$$\frac{\partial \rho_m}{\partial t} + \nabla\bullet\left(\rho_m \mathbf{u}\right) = 0,$$
$$\frac{\partial \rho_m \mathbf{u}}{\partial t} + \nabla\bullet(\rho_m \mathbf{u}\mathbf{u}) = 0, \quad (5)$$
$$\frac{\partial \rho_m E_m}{\partial t} + \nabla\bullet((\rho_m E_m + p_m)\mathbf{u})) = 0,$$

where ρ_m is the medium density, p_m is the pressure, $E_m = e_m + 0.5\mathbf{u}^2$ is the total energy, e_m is the internal energy, and $\mathbf{u}$ is the velocity vector. Here, m indicates mixture of liquid, l, and gas, g, quantities, defined as:

$$\rho_m = \rho_l \alpha_l + \rho_g \alpha_g,$$
$$P_m = \frac{\alpha_l \rho_g c_g^2 P_l + \alpha_g \rho_l c_l^2 P_g}{\alpha_l \rho_g c_g^2 + \alpha_g \rho_l c_l^2}, \quad (6)$$
$$e_m = \frac{1}{\rho_m}\left[\rho_l \alpha_l e_l + \rho_g \alpha_g e_g\right],$$

where α_i is the volume fraction of component i and c_i is the corresponding sound speed.

The liquid-gas mixture density, pressure, and energy are obtained from their components' corresponding values or governing equations. Here, a γ-law (with γ=1.4) is used for air:

$$p_g = (\gamma\text{-}1)\rho_g e_g, \quad (7)$$

and the Tillotson equation is used for water (Zel'Dovich & Raizer 2002):

$$p_l = p_{l,0} + \omega\rho_l(e_l - e_{l,0}) + A\mu + B\mu^2 + C\mu^3,$$
$$\mu = \frac{\rho_l}{\rho_{l,0}} - 1, \quad (8)$$

where ω, A, B, C are constants associated with water and $p_{l,0}$, $e_{l,0}$ and $\rho_{l,0}$ are the reference pressure, specific internal energy, and density respectively. The following default values for water were used in the computations:

$$\rho_{l,0} = 1000 \text{ kg/m}^3,\ \omega = 0.28,\ A = 2.20\times10^9 \text{ Pa},$$
$$B = 9.54\times10^9 \text{ Pa}, \quad C = 1.48\times10^{10} \text{ Pa}, \quad (9)$$
$$e_{l,0} = 3.54\times10^5 \text{ m}^2/\text{s}^2, \quad p_{l,0} = 1.0\times10^5 \text{ Pa}.$$

The compressible flow solver uses a high order predictor-corrector method based on the Monotonic Upwind Scheme for Conservation Law (MUSCL) for pure cells calculations. The solver GEMINI was developed by NSWCIH (Wardlaw & Luton, 2003) and a similar solver was added to the DYNAFLOW 3DYNAFS suite (Kapahi *et al.*, 2015). In the predictor step, cell edge properties at the half step are computed using the method of characteristics. These properties are used to construct a Riemann problem at each cell edge. The procedure to handle the Riemann problem generates different solutions (or "regions"). A "region" corresponding to the location of the cell edge is selected as the solution to cell edge properties. These properties are used to compute the fluxes across each computational cell. The overall predictor-corrector method consists of a slope (of the primitive variables) calculation step, a method of characteristic-based predictor step, and a corrector step involving a Riemann solver. This is a well-established algorithm and details corresponding to each step are provided in (Kapahi *et al.*, 2015) .

The standard MUSCL scheme is augmented by the mixed cell approach to handle material interfaces. For multiple materials, the single fluid algorithm advances the solution first by using temporal average properties. The cells containing the material interfaces and their immediate neighbors known as "mixed cells" are revisited and re-solved using a fully conservative "Lagrange plus remap" step. In the Lagrange step, cell edges that are adjacent to mixed cells are moved at local fluid velocities approximated by the previously computed Riemann slip velocity (corrector step), while edges with pure cells on both sides are held fixed (Kapahi et al. 2015, Wardlaw & Luton 2003). Thus, mixed cells are treated from the Lagrange point of view, while adjacent pure cells have one edge that moves at the local fluid velocity and a stationary one. During the re-map step, the convected flow is mapped back to the original grid.

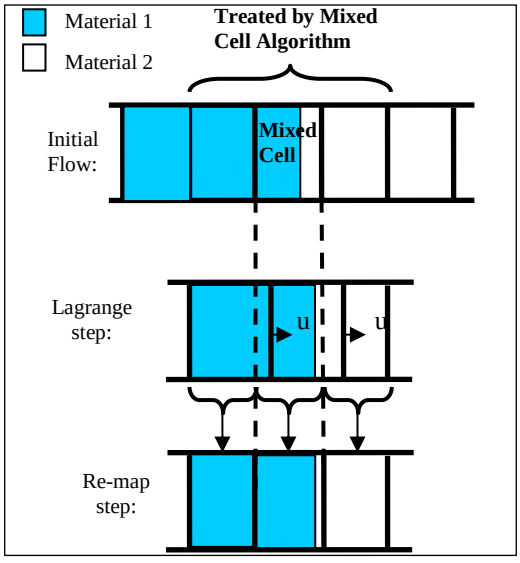

The process is illustrated in Figure 5.

Figure 5. Mixed cell algorithm procedure.

Structure dynamics solver

To model the dynamics of the material, the finite element model DYNAN_2D is used (Whirley & Engelmann, 1993). DYNAN_2D is a non-linear explicit structure dynamics code developed by the Lawrence Livermore National Laboratory. Here it computes the material deformation when the loading is provided by the fluid solution. DYNAN_2D uses a lumped mass formulation for efficiency. This produces a diagonal mass matrix **M,** to express the momentum equation as:

$$\mathbf{M}\frac{d^2\mathbf{x}}{dt^2} = \mathbf{F}_{\text{ext}} - \mathbf{F}_{\text{int}}, \tag{10}$$

where $\mathbf{F}_{\text{ext}}$ represents the applied external forces, and $\mathbf{F}_{\text{int}}$ the internal forces. The acceleration, $\mathbf{a} = d^2\mathbf{x}/dt^2$ for each element, is obtained through an explicit temporal central difference method. Additional details on the general formulation can be found in (Whirley & Engelmann, 1993).

Material models

In the present study, Polyurea and Agar at concentrations of 0.5% and 5% are considered. Both Polyurea and Agar are modeled as viscoelastic materials. In the standard DYNA-N model (Key, 1974), the deviatoric stresses of a viscoelastic material are found from

$$s_{ij}(t) = 2\int_0^t G(t-\tau)D_{ij}^{'}d\tau, \tag{11}$$

where $D_{ij}^{'}$ is the deviatoric strain rate and the function $G(t)$ describes the shear relaxation behavior over time

$$G(t) = G_\infty + (G_o - G_\infty)e^{-\beta t}. \tag{12}$$

The volumetric response is elastic, so the pressure p is computed from the current volumetric strain using

$$p = -K\varepsilon_{Vol}, \tag{13}$$

where K is the elastic bulk modulus and ε_{Vol} is the volumetric strain. In the above equations, G_∞ is the long-time shear modulus, G_o is the short-time shear modulus, and β is a decay constant. While the elastic constants K and G_o used in the simulations are described in Table 1, the decay constant used in the simulation is $4\text{x}10^{-5}$ and the ratio G_0 / G_∞ is 2.0.

Initialization of bubble computations

In order to initialize the bubble dynamics in the compressible code, we have considered two options. One was to simulate the spark as a micro-explosion and use an approach validated for regular explosives to initiate the bubble. This requires a fraction of microgram of TNT. The approach works well but additional work is needed to validate it. Instead, we selected the second method, where the initial phase of the spark generation is ignored, and the bubble dynamics is initiated using a highly compressed gas (here air) in an initially small spherical bubble. This is a common approach in the bubble dynamics literature starting with the Rayleigh-Plesset equation (Rayleigh, 1917 ; Plesset, 1964) and including actually modeling underwater explosion bubbles with potential flow codes (Hsiao & Chahine, 2015). The initial conditions inside the bubble involve unknown very high pressure, $P_{g0,}$ and initial radius R_0. Further, the compressible code requires the initial energy or the initial density of the gas inside the bubble, which obviously has to be consistent with P_{g0} and R_0. Since these initial conditions will dictate the evolution of the bubble, we have established a procedure to compute these initial conditions correctly in order to ensure a proper bubble evolution.

The maximum radius that the bubble expands to, R_{max}, is known from the experiments along with ambient pressure P_{amb}. We first assume an initial radius R_0 and compute P_{g0} using the following relation derived from the Rayleigh-Plesset equations (Krieger & Chahine, 2003):

$$P_{g0} = \left(P_{amb} - P_v\right)\frac{(1-k)\left(1-\varepsilon^{-3}\right)}{1-\varepsilon^{3k-3}}, \qquad \varepsilon = \frac{R_0}{R_{max}}, \tag{14}$$

where P_v is the liquid vapor pressure. The gas is assumed to be ideal and to follow a gas compression law with coefficient k,

$$P_{g,ref}R_{ref}^{\ 3k} = P_{g0}R_0^{\ 3k}. \tag{15}$$

Here, we use k=1.4 and compute the radius corresponding to a reference condition. Knowing the isentropic relation between density and volume at reference conditions and initial conditions, the initial density inside the bubble is then computed. The P_{g0} computed from the above equation does not account for compressible effects and does not account for shock energy losses during the initial bubble expansion. Hence, the value of P_{g0} is changed iteratively in the solution of the fully compressible code in order to obtain the desired R_{max} starting with the isentropic P_{g0} as an initial guess.

FSI model validation with spark experiments

The FSI model described above is first validated by comparison against spark experiments. We present below results obtained at two different non-dimensional standoff distances $\bar{X}$ = 1.52 and 1.05.

The spark generated bubble tests were conducted at low ambient pressure, $P_{amb} \simeq 0.014$MPa, using a 19 mm thick layer of 5% concentration of Agar over a 12.7 mm thick Plexiglas substrate (assumed

fully rigid). The bubbles generated under these conditions were of the order of 20 mm and were easy to visualize with a high-speed camera operating at framing rates of the order of 10,000 fps. Figure 6 shows in black symbols the bubble equivalent radius and in red symbol the displacement of the center of the Agar water interface. Also shown in the figure are the comparative results from the FSI simulations which used the material properties for 5% Agar shown in Table 1. An excellent agreement for the bubble equivalent radius and a very good agreement of the vertical displacement of the center of the square Agar plate-water interface can be seen.

Following initiation of the bubble growth, a high pressure wave is emitted from the spark center and this results in a delayed response of the material, which achieves maximum compression after a response time, τ_m, which depends on the Young modulus and the thickness of the Agar layer (Kulik, 2007). A second large compression results after the collapse of the bubble and the impact of the reentrant jet at the material-water interface. The loading due to the re-entrant jet impingement is one of the main causes of material failure and cavitation erosion (Kim et al., 2014). Excellent comparison is obtained for these two compression events at t = 1 ms and 9.5 ms.

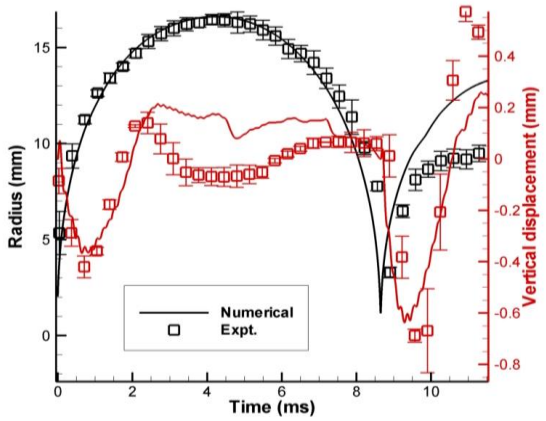

Figure 6: Comparison of bubble equivalent radius and vertical displacement of the Agar layer interface between experiments and simulations: $\bar{X} \sim 1.52$, P_{amb} = 0.014 MPa, R_{max} ~ 17 mm; thickness of the 5% Agar layer = 19 mm.

During the bubble growth and close to R_{max}, we can see the largest discrepancy between the simulations. The spark test results for the Agar motion are significant during this stage than computed numerically. So far, we could not identify the reason for this discrepancy, probably related to a combination of experimental uncertainties and uncertainly in the used material properties. We will investigate this further in the future.

Figure 7 illustrates visually the interaction between the bubble and the Agar layer. This is not exactly the same standoff as shown in the Figure 8 but was selected because it captured quite clearly the various important stages of bubble growth and collapse. The first picture shown at t ~ 0.7 ms corresponds to the first trough of the interface deformation curves during fast bubble growth rate. The figure also shows clearly the reentrant jet development (t ~ 9.7 ms) and formation of a well outlined cavitating vortex ring (here ½ of a torus) with a trail of microbubbles highlighting the jet impact on the wall (t ~ 10 ms), then the collapse of the ring at the wall (t ~ 10.3 ms). Here again a relatively large indentation is formed at the wall.

Figure 8 considers a closer standoff distance, $\bar{X}$ = 1.05, between the bubble and the Agar layer than that shown in Figure 6. The conditions in this case are more similar to those corresponding to Figure 7. The figure compares the bubble equivalent radius and the displacement of the Agar-water interface center. Here too, as expected, an excellent agreement is obtained for the radius evolution, the maximum radius and the bubble period. The first trough in the displacement of the Agar layer at 1ms is predicted well. However, while the overall shape of the displacement function during the reentrant jet dynamics is captured quite well, the actual maximum dip in the displacement curve at 9.5 ms is underpredicted. There is also some discrepancy in the maximum bubble volume region. The reason for these discrepancies can be attributed to either the lack of resolution while capturing the re-entrant jet or are due to the validity of the material model at large displacements. Further investigations are being carried out to resolve this issue.

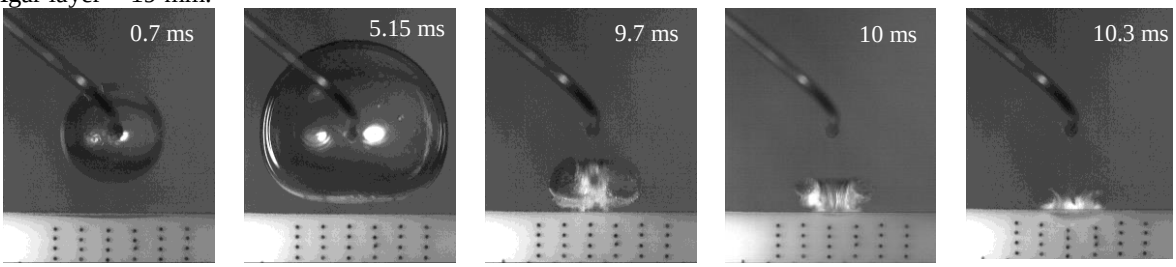

Figure 7. Time sequence of a spark-generated bubble near a 5% Agar plate in a vacuum chamber. $P_{amb} \simeq 0.014$MPa, $\bar{X} \simeq 1$, distance between horizontal dots in material = 5 mm.

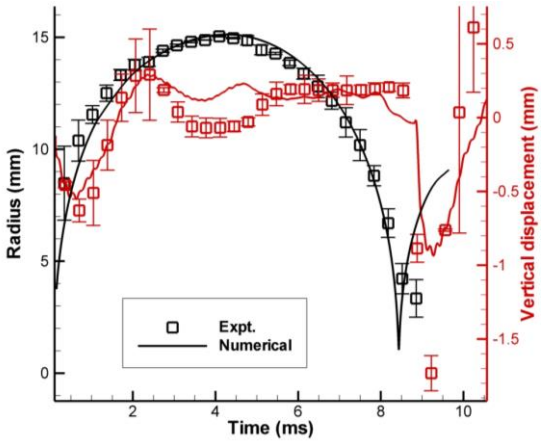

Figure 8: Comparison between experiment and simulations of the bubble equivalent radius and the vertical displacement of the center of the Agar layer interface with water. $\bar{X}$ = 1.05. Spark test conditions: P_{amb} = 0.014 MPa, R_{max} ~ 16 mm; thickness of Agar layer = 19 mm.

Example of improper material scaling

There is a tendency not to realize that one cannot use the same material and scale only the bubble dynamics between the actual cavitation condition and a laboratory larger scale bubble to ease visualization. For instance, to examine the response of Polyurea to microscopic bubble collapse under high pressures, one cannot simply conduct spark-generated bubbles or laser generated bubbles at low pressure and deduce the response through Rayleigh scaling only.

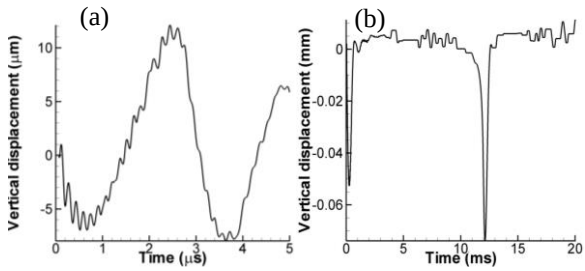

Figure 9: Comparison of the vertical displacements of the interface center point for $\bar{X}$ = 1.0 for Polyurea under (a) Cavitating jet erosive conditions and (b) spark generated bubbles under improper material scaling conditions. Cavitating jet conditions: P_{amb} ~ 7 MPa, R_{max} = 0.1mm; thickness of Polyurea coating = 0.1mm. Spark test conditions: P_{amb} = 0.014 MPa, R_{max} = 20 mm; thickness of Agar layer = 20 mm.

To illustrate this, we compare in Figure 9 the vertical displacement of a 0.1mm thick Polyurea layer due to two largely different size bubbles. Figure 9(b) shows the displacement due to a large 20 mm maximum radius spark-generated bubble growing and collapsing in an ambient pressure of about 0.014 MPa. Figure 9(a) shows the displacement due to a 0.1 mm maximum radius bubble growing and collapsing in an ambient pressure of about 7 MPa. As can be seen in the figures, the small bubble, which also has a very short period, generates a displacement of the Polyurea interface of an amplitude of about 10 μm, while the large, relatively slow dynamics spark bubble, generates two large deformations following the initiation of the dynamics and at bubble collapse respectively and very small deformations in between. One could wrongly conclude from Figure 9 that the spark conditions are more erosive. However, if we follow through with the scaling reasoning, we should compare the results in normalized plots as shown in Figure 10. As expected, the scaling of the bubble radius is very good between the two conditions. It is not perfect due to the terms neglected in the Rayleigh scaling such as the gas pressure inside the bubbles, surface tension, and compressibility effects.

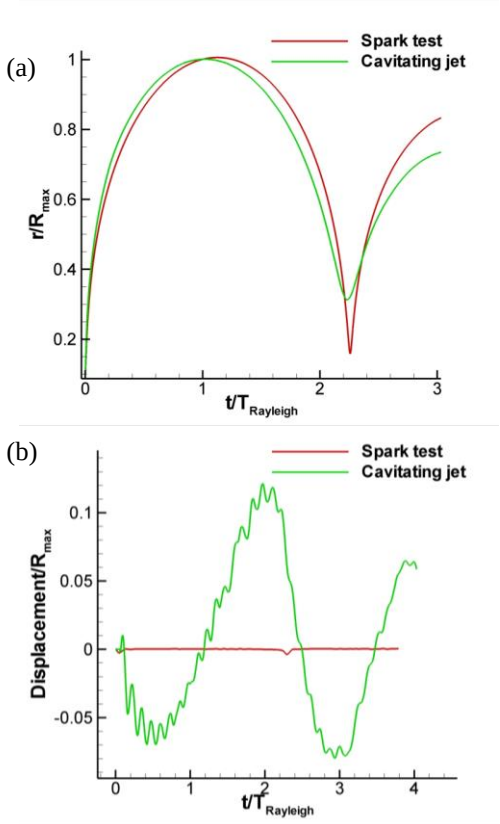

Figure 10: Comparison of (a) the normalized bubble radii and (b) the normalized vertical displacements of the interface center point for the same simulation conditions as in Figure 9.

On the other hand, trying to conclude on the material response based on the spark test is a losing proposition. After normalizing properly, as in Figure 10(b), the spark test material displacement has no connection with the cavitating jet conditions, both in terms of amplitude and qualitative shape of the curves. This highlights again the need to properly scale the material properties and not use the same material, as further demonstrated in the following section.

Examples of proper scaling Polyurea vs. Agar 0.5%

In order to demonstrate a proper scaling, we follow the reasoning presented earlier using Table 1 and Table 2. We recall from Table 2 that in order to simulate a cavitating jet tests at 7 MPa with a spark test at 0.014 MPa, we need for the spark tests a material whose deformation resistance parameters (G and E) are 7/0.014=500 times less than that of Polyurea. As we discussed earlier (see Table 1), a 0.5% concentration Agar possesses such properties. Therefore, we conduct in this section FSI simulations with both Polyurea and 0.5% Agar under the respective conditions and examine the correspondence between the two results.

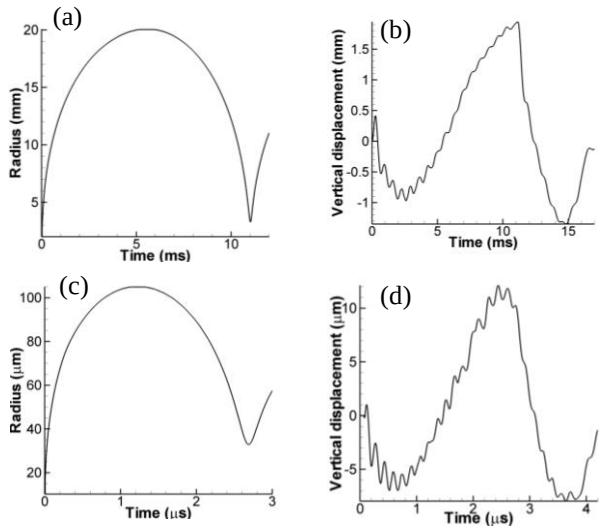

Figure 11: Radius evolution and displacement of the interface center point for $\bar{X}$ = 1.5 for (a), (b) spark-generated bubble conditions, P_{amb}=0.014 MPa, R_{max}~20mm, 0.5% Agar and (c), (d) Bubble collapse in cavitating jet conditions, P_{amb}~7 MPa, R_{max}~100 μm, on Polyurea.

Results of the simulations in both dimensional and non-dimensional formats are shown in Figure 11 through Figure 14 for two non-dimensional standoff distances, $\bar{X}$ = 1.5 and $\bar{X}$ =1.0 respectively. Figure 11 shows the results of the simulation for $\bar{X}$ = 1.5. Figure 11(a) and Figure 11(b) show the time evolution of the bubble equivalent radius and the displacement of the center point of the interface respectively for Agar 0.5%. Figure 11(c) and Figure 11(d) show the same for Polyurea. We can already see that the curves in the two sets have the same shapes and compare qualitatively very well. To compare more appropriately, the bubble equivalent radii are normalized with R_{max} and times with the Rayleigh time and compared together in Figure 12(a). The two sets superpose practically during most of the dynamics and differ by a small amount in the later phase of the collapse. Here too, this discrepancy is due to the terms ignored in the Rayleigh scaling such as the gas pressure inside the bubbles, the surface tension, and compressibility effects, which are different between the two cases.

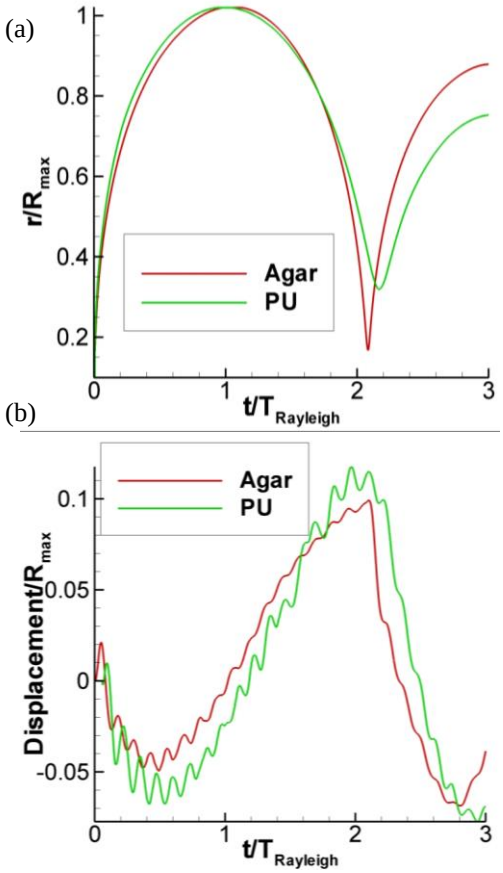

Figure 12: Comparison of (a) the normalized bubble radii and b) the normalized vertical displacements of the interface center point for the same simulation conditions as in Figure 11.

The material interfaces' displacement curves in Figure 12(b), show good correspondence indicating that the dominant physical effects occurring in the Polyurea response to a cavitation bubble collapse are captured very well with the 0.5% Agar both in terms of amplitude and timing. This shows that the procedure can be quite successful.

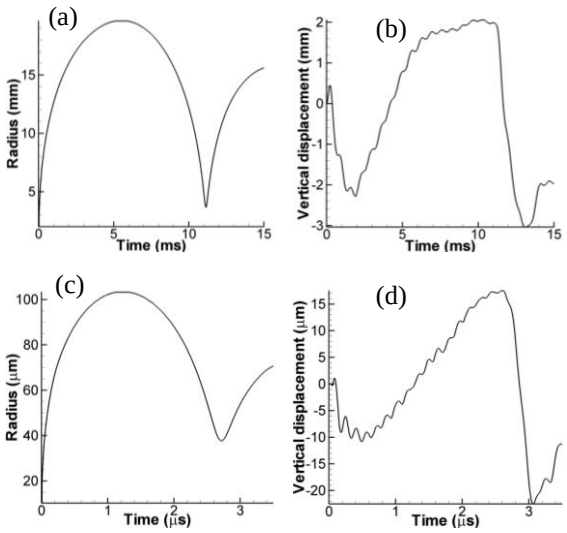

Figure 13: Radius evolution and displacement of the interface center point for $\bar{X}$ = 1.0 for (a), (b) spark-generated bubble conditions, P_{amb}=0.014 MPa, R_{max}~20mm, 0.5% Agar and (c), (d) Bubble collapse in cavitating jet conditions, P_{amb}~7 MPa, R_{max}~100 μm, on Polyurea.

The same procedure is then repeated for a smaller bubble - coating standoff distance, $\bar{X}$ =1.0, and is shown in Figure 13 and Figure 14. Here again we see the same good correspondence between the two scaled configurations. The correspondence between the bubble radii up to the collapse time is very good, while in the later stages of the collapse, interface displacement shows some disagreement due to the physical parameters that are not scaled and also due to the imperfect knowledge of the materials properties.

Effects of the material properties

The material properties of Agar that were used in this study were obtained mainly from the existing literature (Chen, Suki, & An, 2003 ; Nayar et al., 2012). However, there definitely are uncertainties in these selections and it is important to quantify the effects of these uncertainties.

The viscoelastic model used in this study requires two elastic properties as input. Here, we specified the elastic bulk modulus and shear modulus, while the Young's modulus and Poisson's ratio were computed from the standard relations for elastic properties. In the following figures we examine the effects of these properties on the results, considering the cases in Figure 6 where we compared simulations and spark tests.

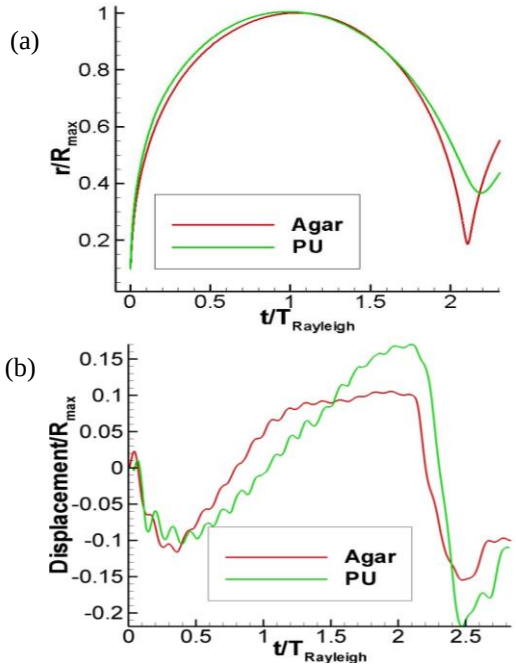

Figure 14: Comparison of (a) the normalized bubble radii and (b) the normalized vertical displacements of the interface center point for the same simulation conditions as in Figure 13.

Figure 15 and Figure 16 illustrate the effect of changing the bulk modulus, *K*, by two orders of magnitude and the shear modulus, *G*, by a factor of 4 respectively. We believe that this exceeds by far any uncertainties.

Since the cases considered here do not involve very strong effects of the material deformation on the bubble dynamics, the evolution of bubble radius versus time is very little affected by changing *K* and *G*, as illustrated in Figure 15. *K* has practically no effect, while increasing *G* appears to have a very small discernable effect. The bubble period elongates by a negligible amount as the material becomes stiffer, which corroborates with our understanding that the bubble period is the longest for a rigid wall. Discernable differences can, however, be observed in Figure 16, which compares the displacement of the center of the interface while changing the material properties. Figure 16(a) shows clearly that the bulk modulus, *K*, has practically no effect, since increasing *K* by two orders of magnitude just damped slightly the oscillations during the time where the bubble was at its

maximum volume. However, these changes did not reduce the discrepancy with the spark tests near R_{max}.

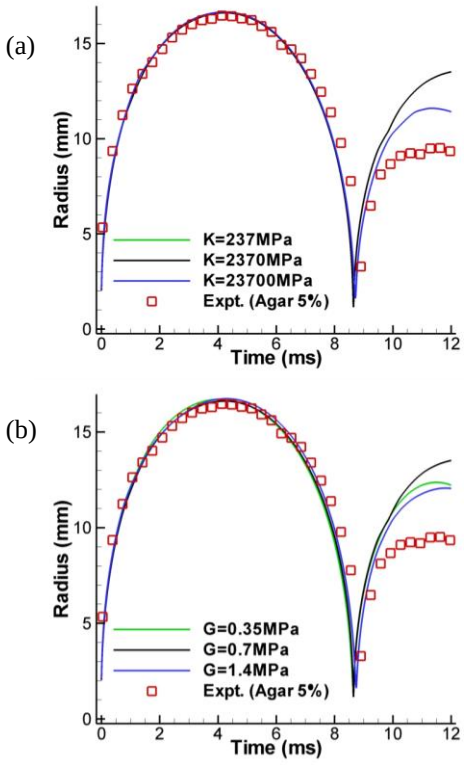

Figure 15: Study of the effects of (a) the elastic bulk modulus, K and (b) the shear modulus G on the bubble equivalent radius time evolution for $\bar{X}$ = 1.5 for Agar 5% under spark test conditions: thickness of Agar layer = 20 mm P_{amb} = 0.014 MPa, R_{max} = 20 mm.

Figure 16(b), on the other hand, shows a measurable effect of the shear modulus, G, (or also the Young's modulus, E, since they are connected) on the response of the Agar layer deformation. Increasing G (thus E) makes the material stiffer and reduces the amplitude of the unsteady material deformations. It also measurably reduces the material response time and reduces the time delay between the source of the excitation (initial pressure pulse and collapse pulse) and the corresponding maximum large deformation.

CONCLUDING REMARKS

The study, presented in this paper, shows that it is possible to properly simulate experimentally the FSI problem of the interaction between a cavitation bubble and a coating layer using different but appropriately selected fluid and material conditions. For instance, a larger and slower spark-generated bubble can be used to conduct visualizations and measurement to represent in a scaled fashion microscopic bubbles collapsing in a high jet pressure environment. To do this, the lengths are scaled using the bubble maximum equivalent radius, R_{max}, while times are scaled with the Rayleigh time. In addition, the materials' Young's moduli and shear moduli ratios have to be scaled by the maximum pressure generated at collapse of the bubble.

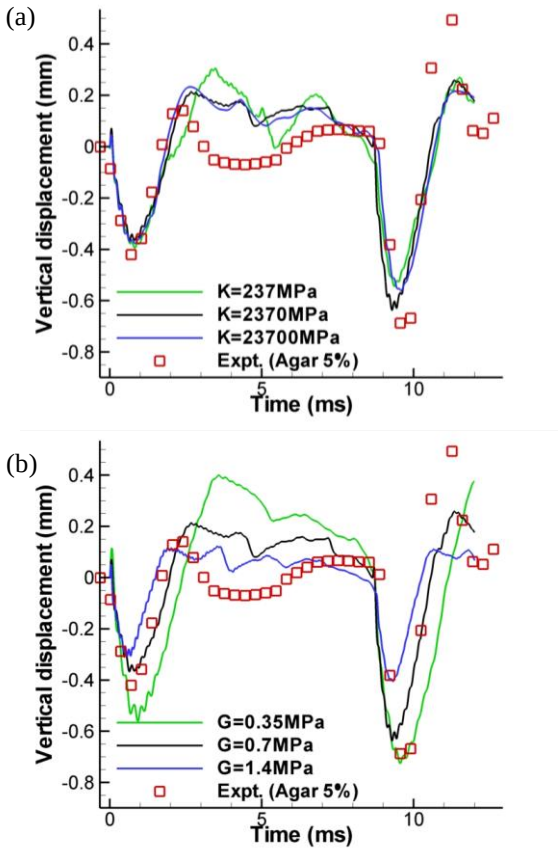

Figure 16: Effects on the displacement of the center of the interface between Agar and water of: (a) the elastic bulk modulus, K and (b) the shear modulus G. $\bar{X}$ = 1.5, thickness of 5% Agar layer = 20 mm, spark test conditions: P_{amb} = 0.014 MPa, R_{max} = 20 mm.

To demonstrate this, spark-generated bubbles and numerical simulations involving fully coupled fluid structure interaction were used to demonstrate the scaling approach. The numerical FSI method was first validated against the spark-generated bubbles and was found to produce a very good agreement. The method was then used to demonstrate the validity of the scaling approach involving scaling both the liquid and bubble dynamics and the material dynamics. Micrometer size cavitating bubbles in a high ambient pressure on a layer of Polyurea coating were shown to have very good correspondence with centimetre size spark generated bubbles on an Agar layer in low ambient pressure. The factors that act as impediments

to achieve perfect scaling were discussed and the effect of uncertainties in the material properties used in the simulations were investigated.

ACKNOWLEDGEMENTS

This work was supported by the Office of Naval Research under contract N00014-15-C-0052 monitored by Dr. Ki-Han Kim. We sincerely appreciate this support.

REFERENCES

Amirkhizi, A. V., Isaacs, J., McGee, J., & Nemat-Nasser, S. "An experimentally-based viscoelastic constitutive model for polyurea, including pressure and temperature effects," Philosophical Magazine, 2006.

Brennen, C. E. "Cavitation and bubble dynamics," Oxford University Press, 1995.

Chahine, G. L. "Modeling of Cavitation Dynamics and Interaction with Material," in A. Kim, K-H, Chahine, G.L., Franc, J-P., Karimi (Ed.), Advanced Experimental and Numerical Techniques for Cavitation Erosion Prediction Springer, 2014, pp. 123‐173.

Chahine, G. L., Franc, J.-P., & Karimi, A., "Laboratory Testing Methods of Cavitation Erosion," in K.-H. Kim, G. L. Chahine, J.-P. Franc, & A. Karimi (Eds), Advanced Experimental and Numerical Techniques for Cavitation Erosion Prediction, Springer, 2014 pp. 21‐36.

Chahine, G. L., Frederick, G. S., Lambrecht, C. J., Harris, G. S., & Mair, H. U. "Spark Generated Bubbles as Laboratory-Scale Models of Underwater Explosions and their use for Validation of Simulation Tools," in 66th Shock & Vibration Symposium, Vol. 2, 1995, pp. 265‐276. Biloxi, MS.

Chahine, G. L., & Hsiao, C.-T. "Modeling Cavitation Erosion via Bubble–Material Interaction," Interface Focus, *5*(5), 2015.

Chen, Q., Suki, B., & An, K.-N. "Dynamic mechanical properties of Agarose gel by a fractional derivative model," in ASME Summer Bioengineering Conference, 2003, Key Biscayne, FL.

Choi, J.-K., & Chahine, G. L. "Experimental and Numerical Study of Polyurea Failure under Cavitation," in SMP 17, 2017, Espoo, Finland.

Cole, R. H. "Underwater explosions," Princeton University Press, 1965, Princeton, New Jersey.

Ellis, A. T. "Parameters Affecting Cavitation and Some New Methods for Their Study - Final Report," California Institute of Technology, October 1965.

Hammitt, F. G. "Cavitation and multiphase flow phenomena," McGraw-Hill,1980.

Hsiao, C.-T., & Chahine, G. L. "Dynamic response of a composite propeller blade subjected to shock and bubble pressure loading," Journal of Fluids and Structures, Vol. 54, 2015, pp. 760–783.

Jayaprakash, A., Chahine, G. L., & Hsiao, C.-T. "Numerical and Experimental Study of the Interaction of a Spark-Generated Bubble and a Vertical Wall," ASME Journal of Fluids Engineering, 134(3), 2012, pp. 31301‐31312.

Kapahi, A., Hsiao, C., & Chahine, G. "A multi-material flow solver for high speed compressible flows," Computers & Fluids, Vol. 54, 2015, pp. 760–783.

Key, S. W. "A finite element procedure for the large deformation dynamic response of axisymmetric solids," Computer Methods in Applied Mechanics and Engineering, 4(2), 1974, pp. 195‐218.

Kim, K.-H., Chahine, G. L., Franc, J.-P., & Karimi, A. Advanced Experimental and Numerical Techniques for Cavitation Erosion Prediction, Springer, 2014.

Kling, C., "A high speed photographic study of cavitation bubble collapse," Thesis University of Michigan,1970.

Kling, C. L., & Hammitt, F. G.,"A Photographic Study of Spark-Induced Cavitation Bubble Collapse," Journal of Basic Engineering, 1972.

Krieger, J. R., & Chahine, G. L., "Dynamics and Acoustic Signature of Non-Spherical Underwater Explosion Bubbles," in 74th Shock and Vibration Symposium, 2003, San Diego.

Kulik, V. M., "Forced oscillations of a layer of a viscoelastic material under the action of a convective pressure wave," Journal of Applied Mechanics and Technical Physics, *48*(2), 2007, pp. 221‐228.

Lord Rayleigh, "On the pressure developed in a liquid during the collapse of a spherical cavity," Philosophical Magazine Series *6*, *34*(200), 1917, pp. 94‐98.

Movahed, P., Kreider, W., Maxwell, A. D., "Hutchens, S. B., & Freund, J. B., "Cavitation-induced damage of soft materials by focused ultrasound bursts: A fracture-based bubble dynamics model," The Journal of the Acoustical Society of America, *140*(2), 2016, pp. 1374‐1386.

Nayar, V. T., Weiland, J. D., Nelson, C. S., & Hodge, A. M. "Elastic and viscoelastic characterization of Agar," Journal of the mechanical behavior of biomedical materials, *7*, 2012, pp. 60‐68.

Plesset, M. S. "Bubble dynamics," in R. Davies (Ed.), Cavitation in real liquids,1964, pp. 1‐17.

Snay, H. G., & Christian, E. A., "Underwater explosion phenomena: the parameters of non-migrating bubble oscillating in an incompressible medium," Navord Report 2437, 1 Feb. 1952.

Wardlaw, A., & Luton, J. A., "The Gemini Euler solver for the coupled simulation of underwater explosions," NSWCIH Technical Report, 2500, 2003.

Whirley, R. G. G., & Engelmann, B. E. E. "DYNA3D: A nonlinear, explicit, three dimensional finite element code for solid and structural mechanics - User manual," Lawrence Livermore National Laboratory, 1993.

Zel'Dovich, Y.B. and Raizer, Y.P., "Physics of shock waves and high-temperature hydrodynamic phenomena," Courier Corporation, 2012.